Effects of Rare Earth Element Additions on the Impression Creep Behavior of AZ91 Magnesium Alloy

F. KABIRIAN and R. MAHMUDI

The effects of 1, 2, and 3 wt pct rare earth (RE) element additions on the microstructure and creep behavior of cast AZ91 Mg alloy were investigated by impression tests. The tests were carried out under constant punching stress in the range 200 to 650 MPa at temperatures in the range 425 to 525 K. Analysis of the data showed that for all loads and temperatures, the AZ91-2RE alloy had the lowest creep rates and, thus, the highest creep resistance among all materials tested. This is attributed to the formation of $Al_{11}RE_3$ with a branched morphology, reduction in the volume fraction of the eutectic β-$Mg_{17}Al_{12}$ phase, and solid solution hardening effects of Al in the Mg matrix. The stress exponents and activation energies were the same for all alloy systems studied, 5.3 to 6.5 and 90 to 120 kJ mol^{-1}, respectively, with the exception that the activation energy for the AZ91-3RE system was 102 to 126 kJ mol^{-1}. An observed decreasing trend of creep-activation energy with stress suggests that two parallel mechanisms of lattice and pipe diffusion-controlled dislocation climb are competing. Dislocation climb controlled by dislocation pipe diffusion is controlling at high stresses, whereas climb of edge dislocations is the controlling mechanism at low stresses.

I. INTRODUCTION

AN excellent combination of superior castability, good corrosion resistance, and acceptable mechanical properties is the main reason for the great attention paid to Mg-Al alloys. In these alloys, aluminum contents in excess of 2 wt pct result in the formation of a network of $Mg_{17}Al_{12}$ precipitates along grain boundaries.[1,2] Due to their low melting point, which ranges from 731 K maximum to the eutectic temperature between the precipitates and Mg, 710 K, these precipitates are thermally unstable and, thus, they can accelerate grain boundary diffusion, resulting in considerable instability of the microstructure in regions adjacent to grain boundaries.[3,4] This makes the high Al-content Mg alloys unsuitable for applications involving high temperature and load. Specifically, their susceptibility to creep limits their allowable temperature to less than 398 K.

The AZ91 alloy containing 9 wt pct Al and 1 wt pct Zn is the most commonly used cast magnesium alloy for low-temperature applications. In this alloy, in addition to the coarsening and dissolution of $Mg_{17}Al_{12}$ precipitates at high temperatures, cellular discontinuous precipitation of this phase can also deteriorate creep resistance during aging. It is believed that this type of precipitation multiplies the grain boundary area, providing more surfaces for easy deformation regimes such as grain boundary sliding at high temperatures.[5] Most of the attempts for improving the creep resistance of this alloy have concentrated on suppressing discontinuous precipitation of $Mg_{17}Al_{12}$ and creating thermally stable intermetallics in the magnesium matrix. For example, the addition of 0.35 wt pct Sb to AZ91 results in the formation of rod-shaped, thermally stable Mg_3Sb_2 intermetallics at grain boundaries, causing significant increase in creep resistance of the alloy.[6] Similarly, Bi addition has been reported to form the thermally stable Mg_3Bi_2, which improves the creep resistance of the AZ91 alloy.[7] Although both Sb and Bi refine the microstructure and suppress the discontinuous precipitation of the β-$Mg_{17}Al_{12}$ phase during aging, they have almost no effect on the volume fraction of $Mg_{17}Al_{12}$ in the as-cast condition.

In contrast to Sb and Bi, there are some other alloying elements such as Zr, Ca, and rare earth (RE), which reduce the amount of the $Mg_{17}Al_{12}$, by consuming the aluminum content of the alloy to form Al-containing intermetallic compounds. Kabirian and Mahmudi[8] studied the effects of Zr additions on the microstructural stability of cast AZ91 after long-time isothermal aging. They showed that the formation of thermally stable Al_2Zr and Al_3Zr_2 particles is accompanied by significant reduction in the volume fraction of the $Mg_{17}Al_{12}$ phase in the as-cast condition. This can significantly hinder grain growth and attain desirable mechanical properties after long-term isothermal aging. A major development in creep-resistant magnesium alloys has been the emergence of RE-containing alloys. This group of alloys contains a mixture of RE elements, containing thermally stable $Al_{11}RE_3$ precipitates. The formation of these branch-shape compounds together with the low diffusion rate of RE elements in Mg matrix can explain the

F. KABIRIAN, Research Assistant, and R. MAHMUDI, Professor, are with the School of Metallurgical and Materials Engineering, University of Tehran, Tehran, Iran. Contact e-mail: mahmudi@ut.ac.ir

excellent creep resistance of RE-containing Mg-Al alloys.[9,10] Pettersen *et al.*[9] studied the effect of 1 wt pct RE on the microstructure of Mg-4Al. Two different kinds of particles, $Al_{11}RE_3$ and $Al_{10}RE_2Mn_7$, were identified at grain boundaries. Observation of $Al_{11}RE_3$ phase from three different angles revealed the connection of parallel laths by crosswise branches. Meanwhile, combining aluminum with RE atoms lowered the level of solute aluminum in Mg matrix in as-cast condition and, consequently, reduced the driving force for discontinuous precipitation of $Mg_{17}Al_{12}$ during creep.

Effects of RE additions on high-temperature mechanical properties of Mg-Al-Zn and Mg-Zn-Al alloys are well documented. Addition of 1 and 3 wt pct RE to AZ91-0.3Ca showed that creep resistance at 473 K had an ascending trend with increasing RE pct, the best high-temperature properties being obtained for 3 pct RE elements.[10] Similar results have been obtained for high-temperature mechanical properties of RE-containing AZ91 and ZA84 alloys.[11–13] Improvement in high-temperature strength has been ascribed to the formation of high melting point $Al_{11}RE_3$ particles as strong barriers to grain boundary sliding. However, coarsening of these particles due to increasing RE pct has been introduced as the major cause for reduction of ultimate tensile strength.[10–12]

There have been many attempts to investigate the possibility of gaining information on creep properties by the use of impression tests.[14–16] Impression creep is a quick, cheap, and effective way of determining creep properties of materials. This test involves applying a constant load to a flat-ended cylindrical punch and recording variations of penetration depth of the indenter as a function of time, from which the penetration rate or impression velocity can be obtained. This can be particularly advantageous when characterizing local material properties and using small specimens for testing, which leads to ease of environmental control and applicability of this technique for testing expensive materials. Using a flat-ended cylindrical punch, compared to standard indenters such as Vickers and Brinell indenters, also has the advantage that in a constant load test, the net section stress under the indenter remains constant, whereas with other indenter geometries, it decreases with time. Furthermore, impression creep avoids problems associated with localized stresses that characterize the tip region during indentation with sharp indenters.[17]

The creep behavior of Mg alloys has been mainly studied by conventional tensile or compressive tests. In a few cases, however, localized creep test methods have been used to evaluate the creep behavior of different magnesium alloys. The creep behavior of AE42, AE41-Ca, and Mg-Sn alloys has been studied by indentation creep using a spherical indenter under constant load.[18,19] The creep behavior of an Mg-8Zn-4Al-0.5Ca alloy in low stress ranges has also been studied by the constant-stress impression creep test.[20] The impression creep behavior of a cast AZ91 alloy has been investigated and compared with those obtained by the conventional tensile creep testing.[21] Using an effective diffusion coefficient, a critical stress was determined, above which the pipe-diffusion mechanism was dominant. The impression creep of AZ91-RE alloys has not been studied before, and thus, the aim of this study is to investigate creep properties of AZ91-RE alloys *via* the impression testing technique.

II. EXPERIMENTAL PROCEDURE

A. *Materials and Processing*

This investigation involved four alloys, which were based on AZ91 (Mg-9 wt pct Al-0.8 wt pct Zn-0.3 wt pct Mn) with 1, 2, or 3 wt pct RE additions. High-purity Mg, Al, Zn, Mn, and a misch-metal mainly composed of La and Ce were used to prepare the alloys. Melting was carried out in an electrical furnace under the MAGREX 36* covering flux to protect molten magne-

---

*MAGREX 36 is a trademark of Foseco, Staffordshire, United Kingdom.

---

sium from oxidation. The melt was held at 1023 K for 20 minutes and mechanically stirred for 2 minutes using a stainless steel rod to ensure a homogenous composition. The melt was then poured into a preheated steel die (573 K), by a tilt-casting technique, in order to minimize casting defects and the turbulence of the melt. The cast slabs had dimensions of $12 \times 20 \times 180$ mm, from which $4 \times 12 \times 20$ mm slices were excised using wire electrodischarge machining. These slices were used for impression creep testing and structural characterization. Scanning electron microscopy (SEM) was used to examine both the as-cast microstructure and the evolution of microstructure after creep. For SEM analysis, the specimens were polished with 0.25-μm diamond paste, followed by polishing on an abrasive-free microcloth. Etching was carried out using an acetic acid–picric acid mixture at room temperature. X-ray diffraction (XRD) and energy-dispersive X-ray (EDX) analysis were carried out on selected samples to identify the phases.

B. *Impression Creep Tests*

The 4-mm slices were tested in an impression tester. The details of the testing arrangement are explained elsewhere[22] and are only briefly described here. An MTS universal tensile testing machine equipped with a three-zone split furnace was used to perform constant-load impression tests. A flat-ended cylindrical punch 2 mm in diameter was mounted in a holder that was positioned in the center of the vertical loading bar. The specimen was located on an anvil below the loading bar, and the assembly of the specimen and the indenter was accommodated by the split furnace. Impression creep measurements were made on each sample under normalized loads (σ_{imp}/G) ranging 0.014 to 0.044 and for dwell times up to 4000 seconds.

After application of the load, the impression depth was measured automatically as a function of time by the machine and the data were acquired by a computer. Using this configuration, it was possible to control the load with the accuracy of 1/20,000 of the load cell nominal capacity of 20 KN, which was ±1 N, and to record the impression depth with the resolution of ±0.001 mm. By controlling the temperature, it was possible to carry out the tests in the temperature range 425 to 525 K. The accuracy of the test temperature in the experimental range 425 to 525 K was within ±0.2 K.

III. RESULTS AND DISCUSSION

Typical impression creep data, presented as the variation of punch penetration depth with dwell time under different normalized stress levels for all materials tested at 455 K, are shown in Figure 1. These curves show that increasing stress at a constant temperature results in higher penetration rates. It can be seen further that after a rather short primary creep stage, almost all of the curves show a relatively long steady-state region where depth increases linearly with time. Since the impression test is essentially compressive in nature, necking and fracture of the specimen do not occur, and hence, it is obviously not possible to record a third stage of the curve, as would be possible in conventional tensile creep testing. It should be noted, however, that some shear stress components may develop in the deformation zone during loading in the impression creep configuration. It is believed that this shear stress is responsible for the impression creep deformation.

Figures 2(a) and (b) show comparisons of impression creep curves under the normalized punching stresses of $\sigma_{imp}/G = 0.032$ at 425 K and $\sigma_{imp}/G = 0.028$ at 455 K, respectively. To make sure that a steady state has been reached, impression velocity $(V_{imp} = dh/dt)$ is plotted against impression depth (h) on a semilogarithmic scale for the AZ91 and AZ91-2RE alloys at $T = 425$ K,
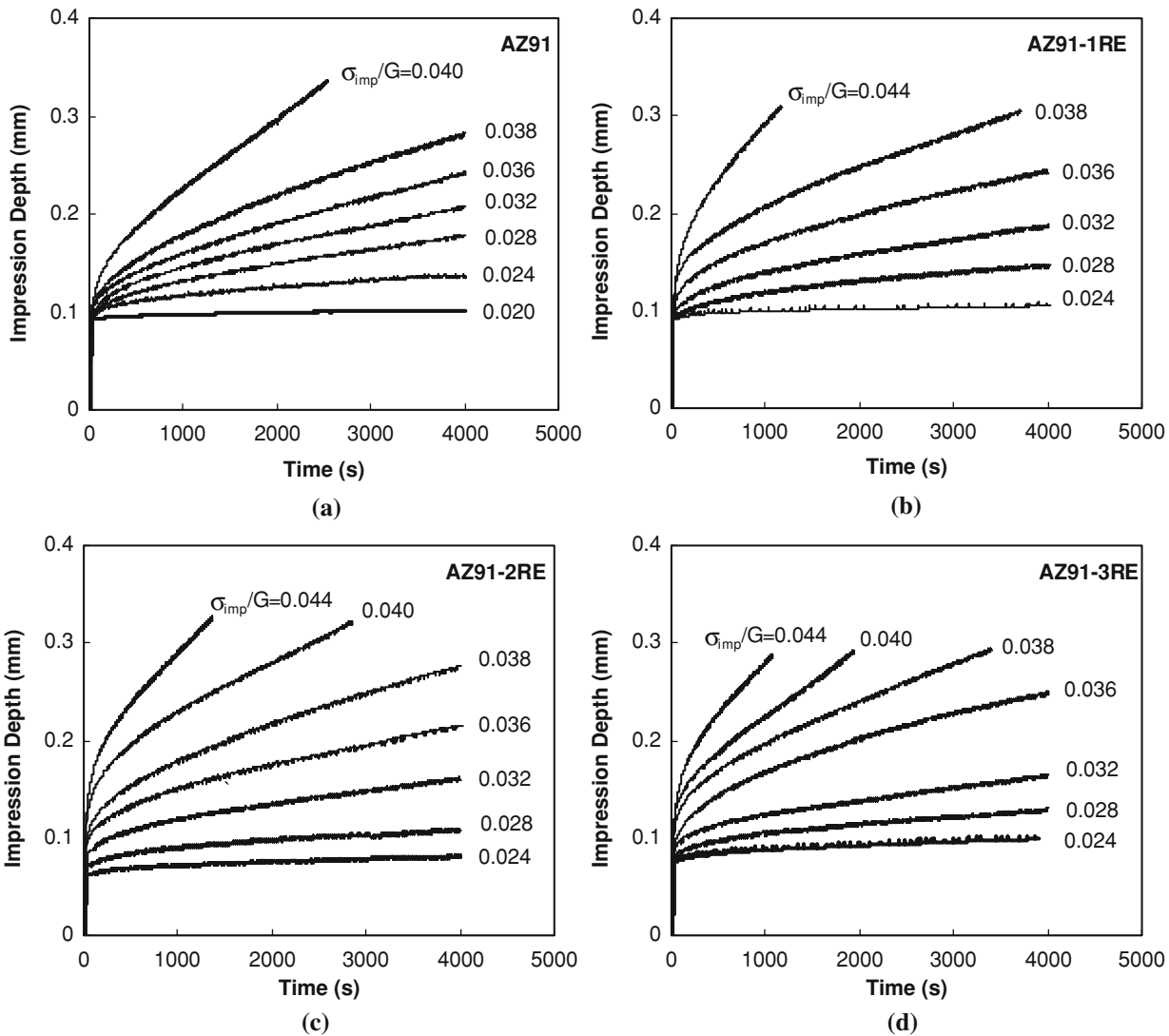

Fig. 1—Typical creep curves of the investigated alloys at 455 K under different σ_{imp}/G levels: (a) AZ91, (b) AZ91-1RE, (c) AZ91-2RE, and (d) AZ91-3RE alloy.
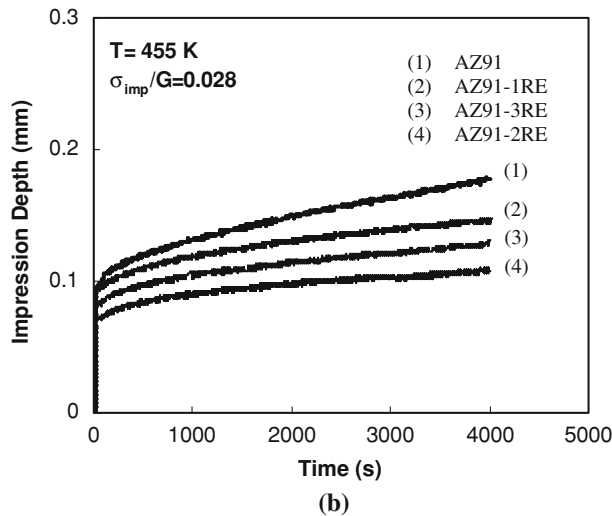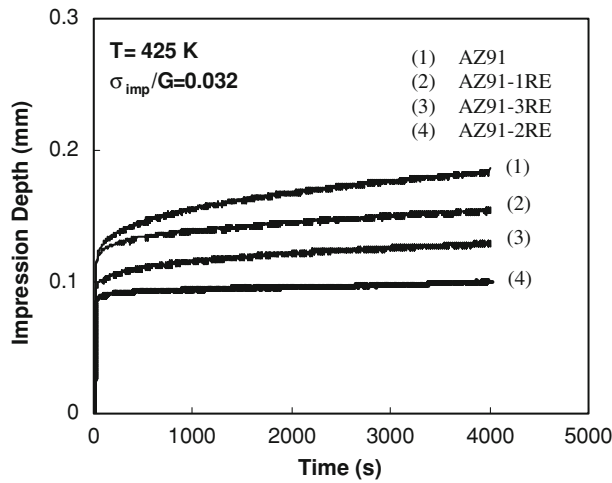
(a)

(b)

Fig. 2—Comparison of creep behavior of the investigated alloys at (*a*) $T = 425$ K, $\sigma_{\text{imp}}/G = 0.032$; and (*b*) $T = 455$ K, $\sigma_{\text{imp}}/G = 0.028$.

(a)

(b)

Fig. 3—Variation of impression velocity with impression depth for AZ91 and AZ91-2RE, showing steady-state impression velocities obtained at (*a*) $T = 425$ K, $\sigma_{\text{imp}}/G = 0.032$; and (*b*) $T = 455$ K, $\sigma_{\text{imp}}/G = 0.028$. Steady-state creep rates are marked with arrows.

$\sigma_{\text{imp}}/G = 0.032$ and $T = 455$ K, $\sigma_{\text{imp}}/G = 0.028$, as shown in Figures 3(a) and (b), respectively. The time derivatives of the $h(t)$ curves were calculated by a five-point cubic spline numerical differentiation computer program. It is observed that there is a steep drop in the impression velocity (V_{imp}) at the beginning of each test (shallow impression depth). The authors attribute this initial high impression velocity to the primary creep stage. It is followed by an almost constant impression velocity region, which presumably corresponds to the steady-state creep stage of the tested materials. The shapes of these curves, especially those for the low creep rate conditions, are very similar to those obtained in compressive creep studies of AZ91 reported by Blum *et al.*[23] The observed varying initial deformations could be due to different work hardening behaviors of the pure AZ91 and AZ91-RE alloys, caused by varying volume fractions of intermetallic particles in the RE-containing materials.

Concerning the reproducibility of the impression creep curves, especially for the cast materials, care must
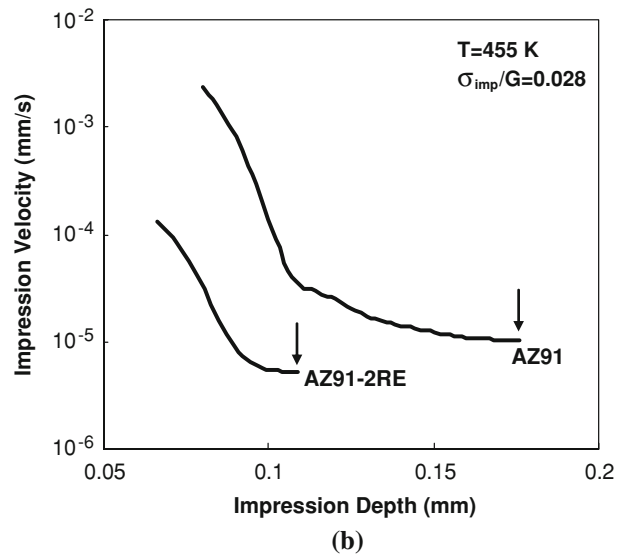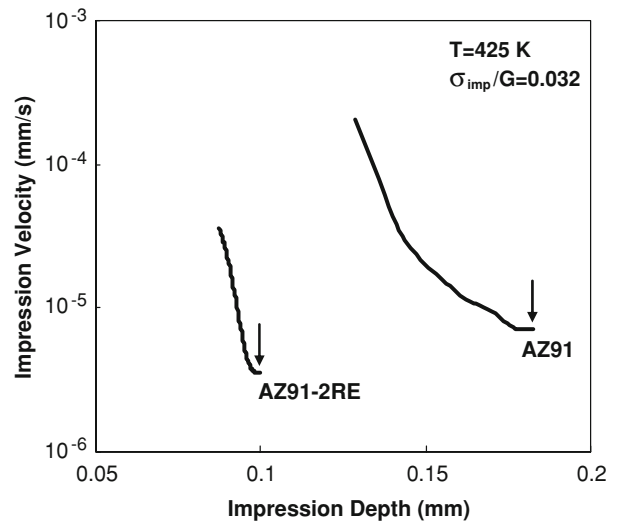
be taken to consider the impact of the comparable sizes of the indenter and defects, grains, and other microstructural constituents. This is likely to cause significant scatter, depending on where the impression is made and how many grains and other constituents contribute to the obtained impression-depth data. If, for example, only a few grains contribute, the data will become dependent on crystallographic orientation. The same is true for the microstructural inhomogeneities and defects, which may be located beneath the indenter, affecting the materials' resistance to impression. In the present work, however, at least three separate measurements were taken at random places on the surface of the specimens for each condition, and the secondary creep rates were almost identical. This may imply that, due to the relatively high cooling rate of the melt imparted by the steel die and also use of a tilt-casting method, a

Table I. Steady-State Impression Creep Data Obtained at Different Temperatures and Stresses

σ_{imp}/G	Temperature (K)	Steady-State Impression Velocity $\times 10^{-6}$ (mm/s)			
		AZ91	AZ91-1RE	AZ91-2RE	AZ91-3RE
0.040	425	18	15	12	16
	455	79	70	63	73
	485	640	330	298	435
	525	—	—	—	—
0.036	425	10	8.0	6.0	9.9
	455	40	34	31	38
	485	—	260	240	—
	525	—	—	—	—
0.032	425	7.9	4.7	3.5	4.2
	455	26	21	20	23
	485	120	99	91	—
	525	—	—	—	—
0.028	425	—	—	—	—
	455	11	8.0	6.0	6.7
	485	49	34	29	40
	525	250	210	197	223
0.024	425	—	—	—	—
	455	4.7	2.6	2.4	3.1
	485	17	16	13	15
	525	157	138	122	135
0.020	425	—	—	—	—
	455	1.5	—	—	—
	485	9.2	6.3	5.5	7.0
	525	51	48	45	56

refined defect-free microstructure has resulted, and hence, the impression creep data bear a high level of reliability.

Another feature of the curves depicted in Figure 2 is that, at both testing temperatures, the introduction of RE into AZ91 generally improves its creep resistance. The lowest level and slope in the steady-state region belong to the AZ91-2RE alloy, the highest to the AZ91 alloy, with the remaining alloys lying between. In other words, the creep resistance increases with the RE content up to 2 wt pct but then decreases for 3 wt pct RE. The steady-state creep rates are summarized in Table I for all four alloys tested at each temperature and stress level.

The authors attribute the observed differences in the impression creep behavior of the alloys to their respective microstructures. Figures 4(a) through (d) show SEM micrographs of AZ91 and the AZ91-RE-containing alloys. The microstructure of AZ91 is basically composed of the network of eutectic β-$Mg_{17}Al_{12}$ distributed in the magnesium matrix, the volume fraction of which decreases in the RE-containing alloys with increasing RE content. This can be attributed to the fact that RE elements consume some of the aluminum by forming Al-RE intermetallic compounds, leaving less aluminum to combine with the Mg matrix to form β-$Mg_{17}Al_{12}$. The affinity of RE atoms for Al is so high that there is no need for preferential nucleation of the $Al_{11}RE_3$ intermetallics. In other words, if the aluminum content of the magnesium matrix is high enough to combine with RE, the formation of RE-containing intermetallics takes place in the interior parts of the

dendrites as well as at the boundaries, assuming that there is sufficient solubility of the RE in the Mg.

It is also notable that there is a change in the morphology of the RE-containing intermetallics as the RE content varies from 2 to 3 wt pct. As can be observed in Figures 4(b) through (d), the increase in the RE content leads to a change in the particle morphology from a branched type in the AZ91-1RE and AZ91-2RE alloys to a coarse acicular shape in the AZ91-3RE alloy. A higher magnification image of the AZ91-3RE alloy, shown in Figure 5(a), contains both acicular Al-RE intermetallics and nodular β-$Mg_{17}Al_{12}$ particles. Qualitative analysis of the needle-shaped particles, determined by the EDX analysis and shown in Figure 5(b), confirms that La, Ce, and Al are the main constituents of such particles.

To identify the phases present in the tested alloys, XRD spectra were obtained and are shown in Figure 6. As can be seen, α-Mg and β-$Mg_{17}Al_{12}$ are the only phases in the AZ91 alloy, whereas in the AZ91-2RE alloy, additional peaks are evident. These new peaks correspond to the $Al_{11}RE_3$ intermetallic compound, which is the main cause for the enhanced creep resistance of the RE-containing alloys. Since the volume fraction of this phase increases with increasing the RE content in the alloys, one would expect the highest creep resistance for the AZ91-3RE alloy. However, the best creep resistance belongs to AZ91-2RE. The authors explain the decrease in creep resistance of AZ91-3RE relative to AZ91-2RE as being the results of the reduction in Al solid solution hardening, because Al has been removed from the Mg matrix by the formation
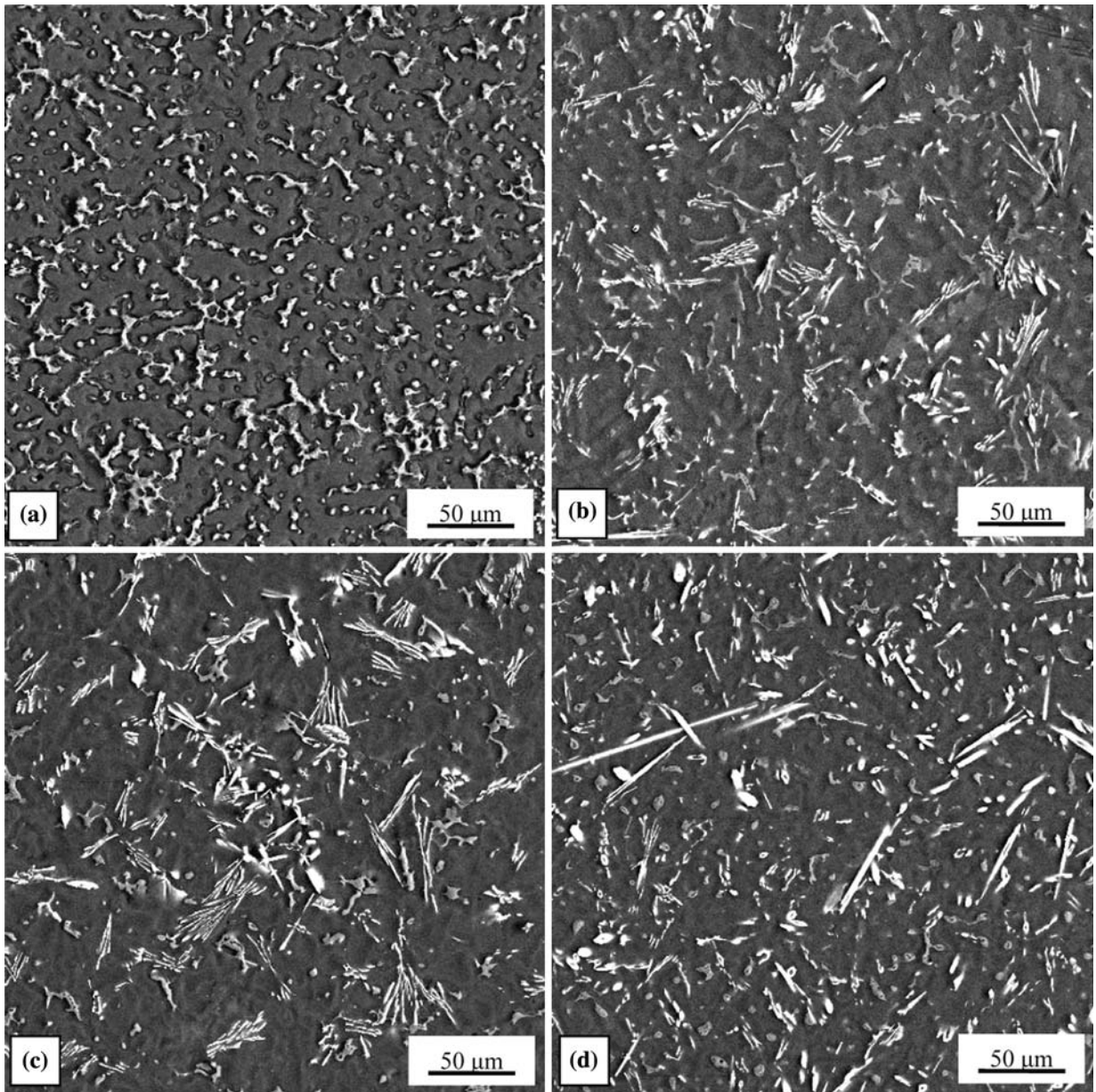
Fig. 4—SEM micrographs of (*a*) AZ91, (*b*) AZ91-1RE, (*c*) AZ91-2RE, and (*d*) AZ91-3RE alloys.

of a higher volume fraction of Al-RE phases. AZ91-2RE would appear to have an optimum balance of strengthening, which benefits from both particle hardening of the fine intermetallics and solid solution hardening effects of Al in the Mg matrix.

In order to study the microstructural evolution of the specimens during impression creep, crept samples were sectioned along the impression direction in the middle of the impressed area, beneath the indenter. Figures 7(a) through (c), respectively, show the microstructural evolution of AZ91, AZ91-2RE, and AZ91-3RE in this location after creep testing at 455 K. Three distinguishable regions are observed. For the benefit of the reader, these are separated from each other by curved lines and are labeled 1, 2, and 3. In region 1, which has an approximately hemispherical shape, no microstructural

changes are detectable for all three alloys. In region 2 of AZ91 (Figure 7(a)), however, the β-$Mg_{17}Al_{12}$ particles are elongated in the direction of material flow, as indicated with a curved arrow. Outside this region, far from the indenter (region 3), there is an almost random distribution of the second phase with no distinguishable flow pattern. Thus, the regions close to and far from the indenter are without microstructural disruption. This implies that the stress state in the regions beneath the indenter is hydrostatic, while in the regions far from the indenter, the material has not undergone any considerable plastic deformation due to the localized nature of the impression creep test.

The alignment in the flow direction of the massive $Mg_{17}Al_{12}$ second phase, shown in Figure 7(a), can be ascribed to the extensive shear deformation taking place
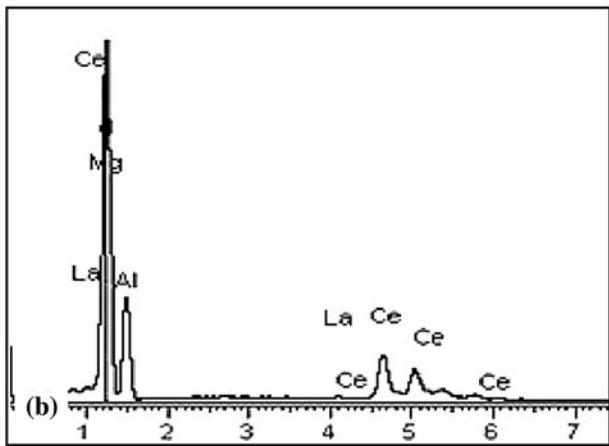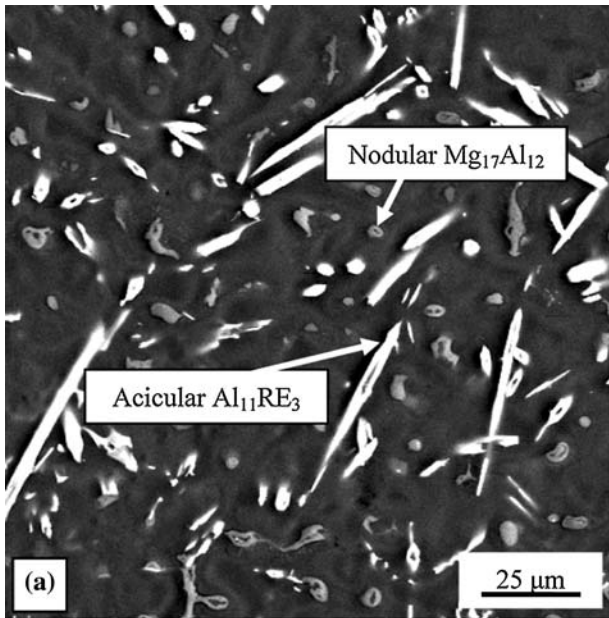
Fig. 5—(a) Illustration of coarse acicular-shape RE-containing intermetallics in the AZ91-3RE alloy. (b) EDX analysis of the same intermetallics.

Fig. 6—XRD patterns of the AZ91 and AZ91-2RE alloys.

below the indenter. The observed substantial deformation could be due to possible softening of β-$Mg_{17}Al_{12}$ particles with increasing temperature beyond 400 K. This leads to weakening of regions adjacent to dendrite boundaries and, consequently, to deterioration of creep properties. The β-$Mg_{17}Al_{12}$ particles cannot hinder dislocation recovery in stress and temperature ranges in which dislocation creep is the dominant creep mechanism. In other words, these particles cannot impede the plastic deformation in the vicinity of dendrite boundaries and easily deform with developing shear stresses.

The microstructure of the AZ91-2RE, shown in Figure 7(b), contains a rather uniform distribution of intermetallics with almost no distinct flow pattern in region 2. This can be attributed to the high thermal stability and strength of the $Al_{11}RE_3$ intermetallic compound, which resists the applied shear stresses in the deformation zone at high temperatures. The lower creep rate, and thus higher creep resistance of the
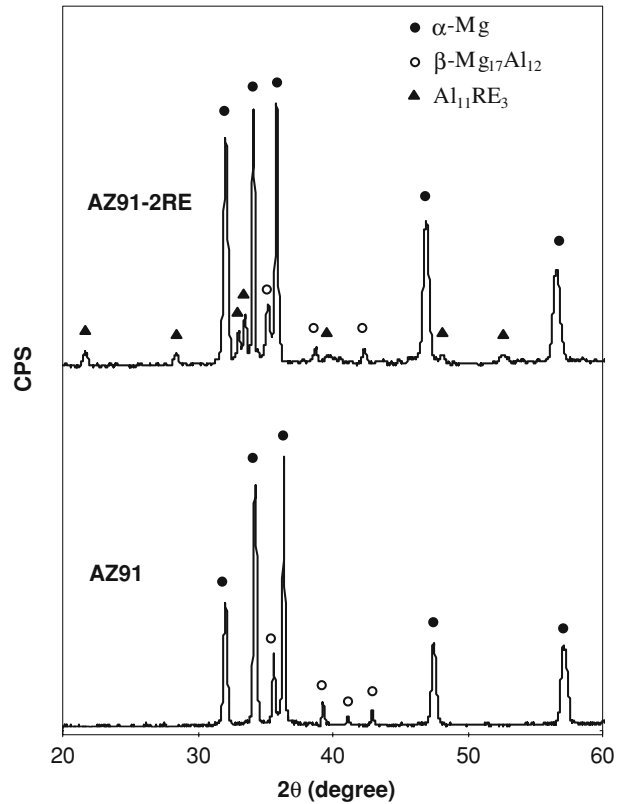
AZ91-2RE alloy, is a direct consequence of this stability and strength. As the level of RE is increased to 3 pct, the volume fraction of the $Al_{11}RE_3$ intermetallics increases, but this leads to a reduction in solid solution hardening, due to the consumption of Al atoms, as proposed previously. These particles cannot apparently resist the applied stress and are thus fragmented, producing a fine and dense distribution of the particles aligned in the flow direction (Figure 7(c)). The easier flow of these particles in an Al-depleted softer matrix results in a reduced creep resistance of the AZ91-3RE alloy, consistent with the data shown in Figure 2. The presence of a softer Mg matrix in the AZ91-3RE alloy has been previously reported in the literature,[12] and in the present work, it can be manifested by the higher density of the Al-RE particles, as shown in Figure 7(c).

It is generally accepted that the steady-state creep rate of a metallic material can be correlated to the applied stress by the well-known power-law equation

$$\dot{\varepsilon} = A\left(\frac{G\mathbf{b}}{kT}\right)\left(\frac{\sigma}{G}\right)^n \exp\left(-\frac{Q_c}{RT}\right) \qquad [1]$$

where A is a material parameter, $\mathbf{b}$ is the Burgers vector, G is the shear modulus, k is the Boltzmann's constant, T is the temperature, σ is the applied stress, n is the stress exponent, Q_c is the creep-activation energy, and R is the universal gas constant.

To correlate the impression and the conventional tensile creep data, the equivalent stress and strain rate can be calculated from the impression velocity
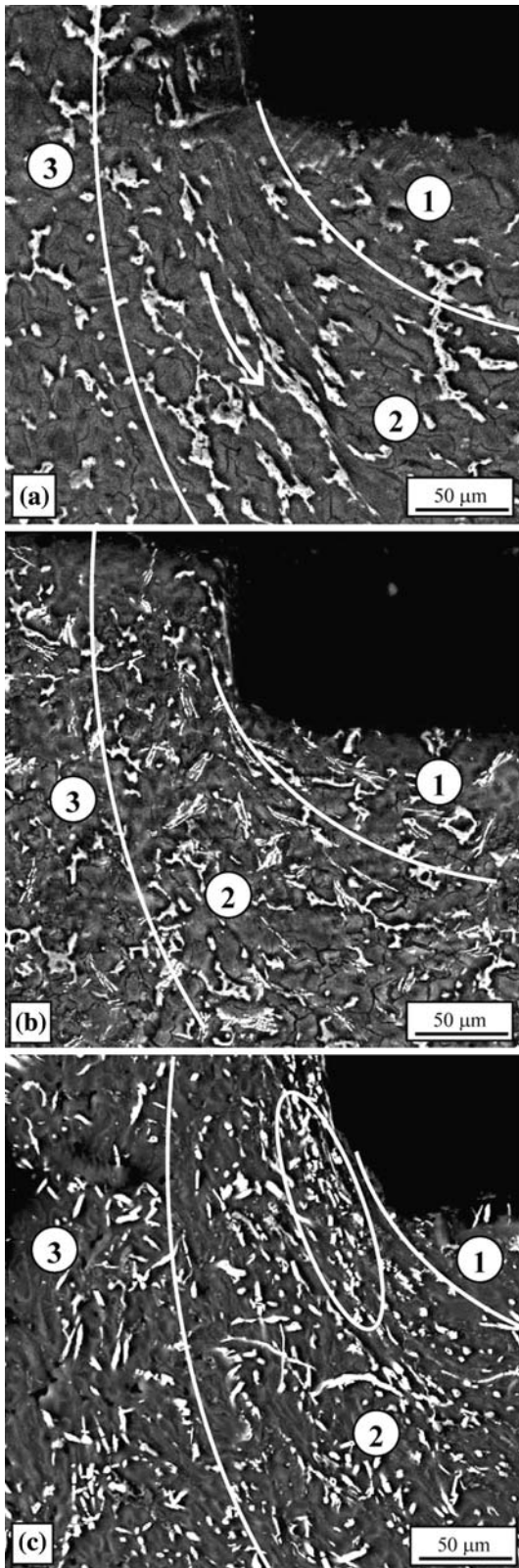
Fig. 7—Cross section of the impression edges after creep at 455 K: (a) AZ91, (b) AZ91-2RE, and (c) AZ91-3RE. The ellipse shows broken rod-shape $Al_{11}RE_3$ intermetallics near the cylindrical impression wall.

$(V_{imp} = dh/dt)$, the impression stress under the punch $(\sigma_{imp} = 4F/\pi\phi^2)$ at a given load F, and the punch diameter ϕ as

$$\sigma = \frac{\sigma_{imp}}{c_1} \text{ and } \dot{\varepsilon} = \frac{dh/dt}{\phi c_2} = \frac{V_{imp}}{\phi c_2} \qquad [2]$$

where c_1 and c_2 are constants. Therefore, inserting Eq. [2] into Eq. [1] and rearranging gives the relationship between impression velocity and applied punch stress:

$$\left(\frac{V_{imp}T}{G}\right) = B\left(\frac{\sigma_{imp}}{G}\right)^n \exp\left(-\frac{Q_c}{RT}\right) \qquad [3]$$

Since B is a constant, it is possible to obtain the stress exponent n from a plot of $\ln(V_{imp}T/G)$ against $\ln(\sigma_{imp}/G)$ at constant T. Similarly, the activation energy Q_c can be obtained from a plot of $\ln(V_{imp}T/G)$ vs $(1/T)$ at constant (σ_{imp}/G). The shear modulus, G, of the AZ91 alloy was calculated from G (MPa) = $18{,}460 - 8.2T$ (K),[24] and the stress exponents were determined according to Eq. [3] by plotting the compensated impression rates against normalized punching stress, as shown in Figure 8. The results, given in Table II, show that the stress exponents decrease, respectively, from 6.0 to 4.9, 6.8 to 5.6, 6.7 to 5.3, and 7.0 to 6.0 for AZ91, AZ91-1RE, AZ91-2RE, and AZ91-3RE, as the temperature increases from 425 to 525 K. The decrease in the stress exponent with increasing temperature observed for all materials suggests the instability of the microstructure, which occurs during the high-temperature creep process.

In order to obtain the activation energy values, the normalized steady-state impression velocities, $V_{imp}T/G$, were plotted against the reciprocal of the absolute temperatures on a semi-logarithmic scale, as shown in Figure 9. The activation energies, calculated from the slopes of these lines $(-Q_c/R)$, show a decrease from 112.6 kJ/mol at $\sigma_{imp}/G = 0.024$ to 94.1 kJ/mol at $\sigma_{imp}/G = 0.036$ for AZ91, and from 110.2 kJ/mol at $\sigma_{imp}/G = 0.024$ to 96.3 kJ/mol at $\sigma_{imp}/G = 0.036$ for AZ91-2RE. A complete set of activation energy data for all four alloys tested at each normalized stress level is tabulated in Table II.

To have a more integrated view of the creep data, the normalized steady-state impression velocity was plotted as a function of normalized punching stress and reciprocal temperature for AZ91 and AZ91-2RE, as shown in Figure 10. In these three-dimensional plots, the creep data are expressed as surfaces that can provide the creep rate for any combination of load and temperature. Obviously, the creep rates have a minimum at the lowest stress and temperature and a maximum at the highest levels of these two variables. The comparison of the creep rates for AZ91 (Figure 10(a)) and AZ91-2RE (Figure 10(b)) indicates the better performance of the latter material, especially in low and medium temperature and stress ranges. As
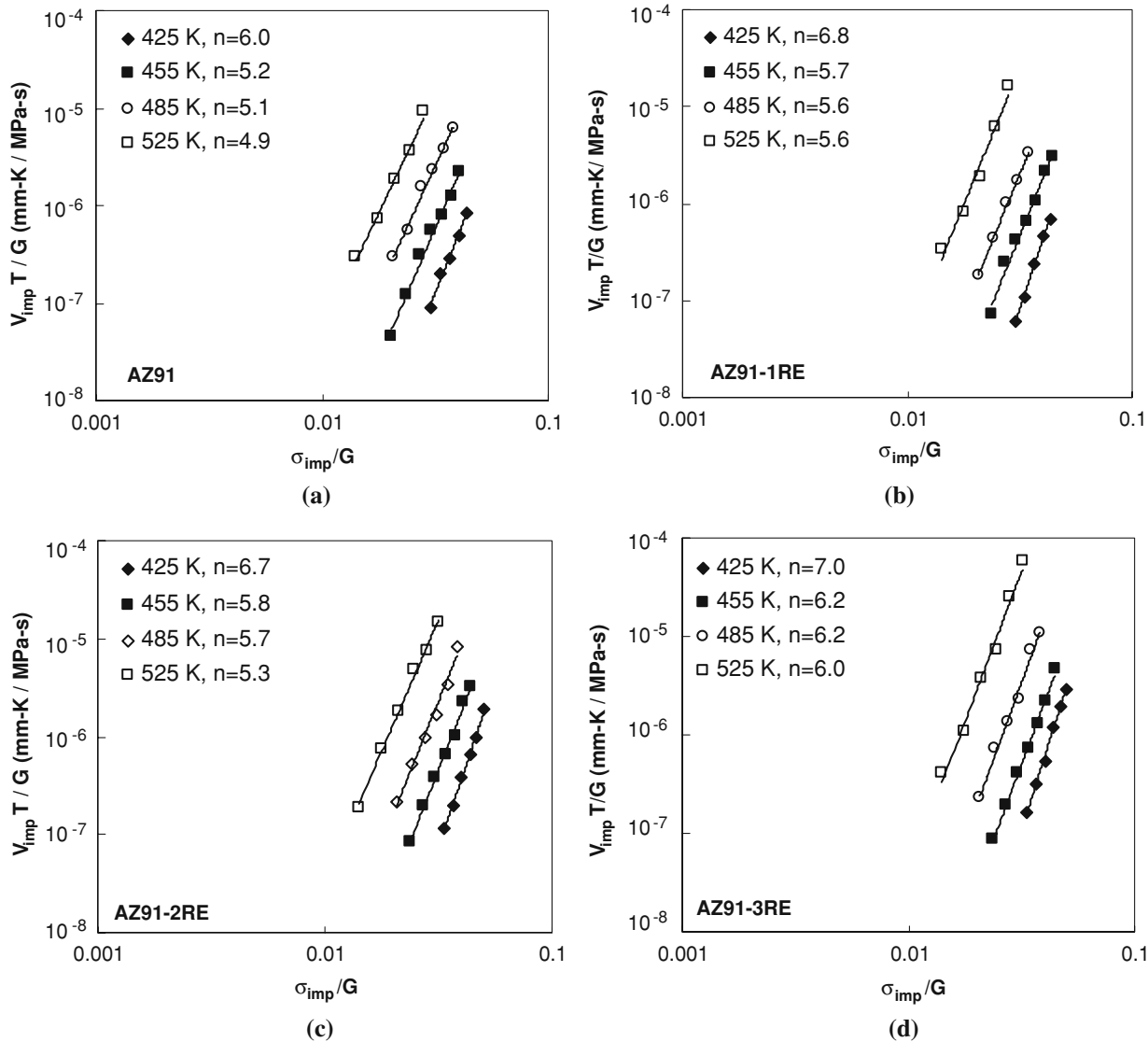
Fig. 8—Normalized steady-state impression velocity as a function of normalized punching stress at different temperatures to determine *n* values for (*a*) AZ91, (*b*) AZ91-1RE, (*c*) AZ91-2RE, and (*d*) AZ91-3RE.

the temperature and stress increase, however, the difference between the creep resistances of the materials becomes smaller.

It is generally accepted that deformation of polycrystalline materials at temperatures above $0.5T_m$ can take place by different deformation mechanisms associated with different stress exponents and activation energies. According to the theory of dislocation-climb-controlled creep, the stress exponent has the value of 5 and the activation energy has the value of the activation energy of lattice self-diffusion.[25] At lower temperatures, dislocation pipe diffusion becomes dominant, in which case the *n* value increases to 7 and the activation energy becomes that of the activation energy for pipe diffusion.[26] The theory of dislocation viscous glide, however, leads to a stress exponent of 3 at high temperatures and 5 at low temperatures, the respective activation energies being those for solute interdiffusion and dislocation pipe diffusion.[27,28]

Table II. Stress Exponents and Activation Energies for the Tested Materials

Alloy	Stress Exponent (*n*)				Activation Energy (*Q*), kJ/mol			
	Temperature, K				σ_{imp}/G			
	425	455	485	525	0.024	0.028	0.032	0.036
AZ91	6.0	5.2	5.1	4.9	112.6	109.7	99.8	94.1
AZ91-1RE	6.8	5.7	5.6	5.6	118.2	117.7	93.9	90.1
AZ91-2RE	6.7	5.8	5.7	5.3	110.2	104.5	104.0	96.3
AZ91-3RE	7.0	6.2	6.2	6.0	125.8	124.5	105.5	102.0

Although the obtained stress exponents of 4.9 to 7.0 are in the range of those for climb of edge dislocations, creep-activation energy values are lower than what is accepted for magnesium lattice diffusion
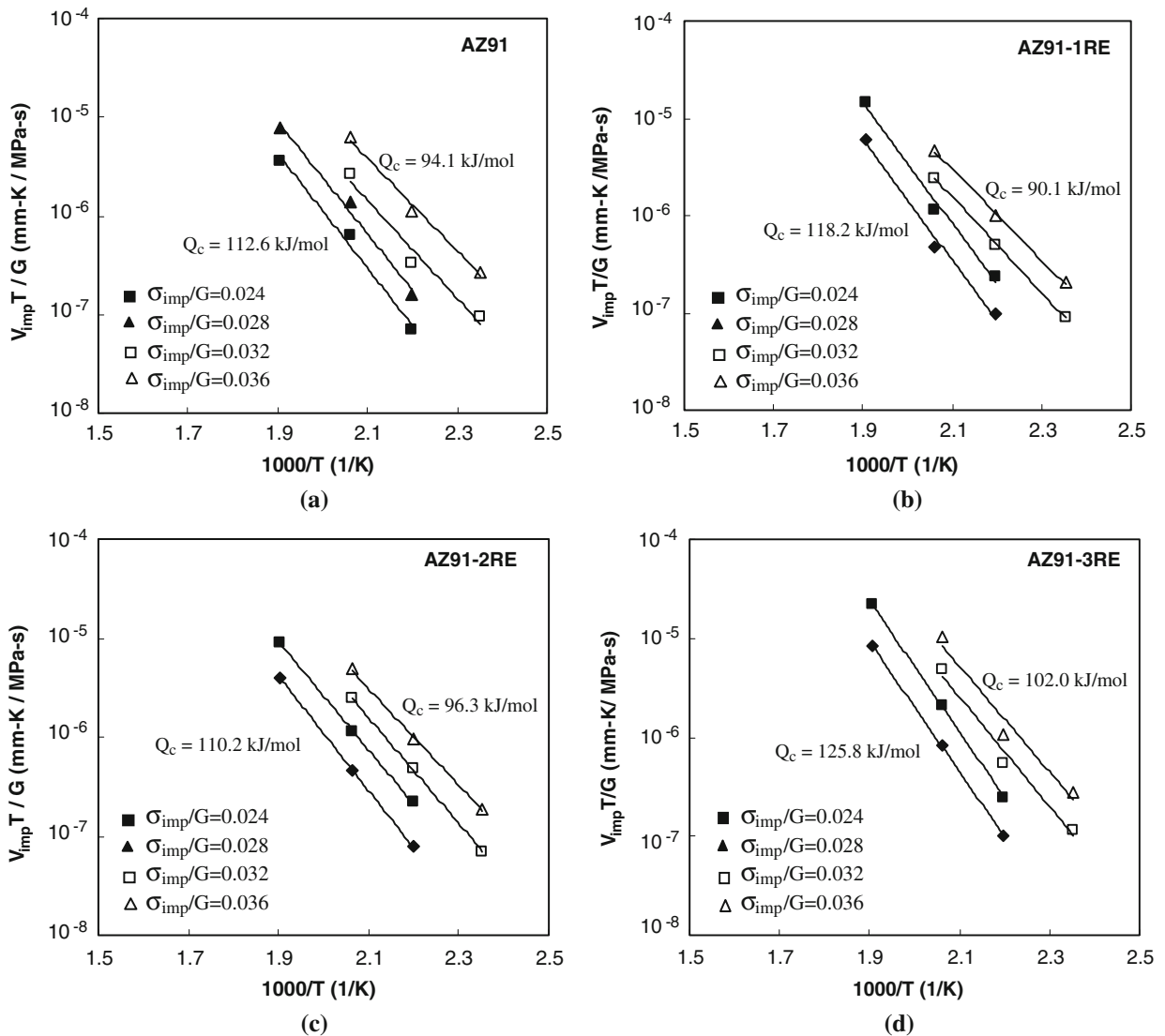
Fig. 9—Plots of the temperature dependence of the normalized steady-state impression velocity at different constant normalized punching stresses to determine Q values for (a) AZ91, (b) AZ91-1RE, (c) AZ91-2RE, and (d) AZ91-3RE.

(Q_l = 135 kJ/mol). Such anomalies in creep-activation energy values have been reported for Mg and its alloys in the literature. It has been shown, for example, that for the coarse-grained AZ91 alloy, the obtained creep-activation energies varied from 94 to 220 kJ/mol in the temperature range 393 to 453 K, while the stress exponent of 11 remained constant.[29] In another study, for AZ91, the activation energy decrease from 171 to 121 kJ/mol with increasing stress from 25 to 45 MPa has also been reported over the temperature range of 547 to 597 K, while the stress exponents remained in the range of 3 to 5.[30] Finally, a similar decrease of creep-activation energy with increasing stress has also been reported for the AM50 alloy, for which the activation energy decreased from 131 to 111 kJ/mol in the stress range where power-law creep prevailed.[31]

The fact that our measured activation energies in the range Q_c = 90 to 125 kJ/mol are lower than the activation energy for magnesium lattice diffusion (Q_l = 135 kJ/mol) may imply that another process parallel to lattice-diffusion-controlled dislocation climb might have been activated. In the case of parallel creep processes, each process contributes to the overall creep strain, but the faster one controls the steady-state creep rate. One of the major events that leads to $Q_c < Q_l$ is the simultaneous activation of lattice and pipe diffusion processes. The contribution of pipe diffusion to the overall diffusion process has been investigated for the cast AZ91 alloy.[21]

Based on the idea that there exists a transition temperature between pipe diffusion and lattice-diffusion-controlled creep, suggested by Sherby and Burke,[32] it has been proposed that the activation energy of lattice self-diffusion (Q_{ld}) is related to the pipe diffusion activation energy (Q_{pd}) by the relationship $Q_{pd} = 0.7Q_{ld}$.[26] If correct and assuming a lattice diffusion activation energy of Q_{ld} = 135 kJ/mol, then the activation energy for pipe diffusion of
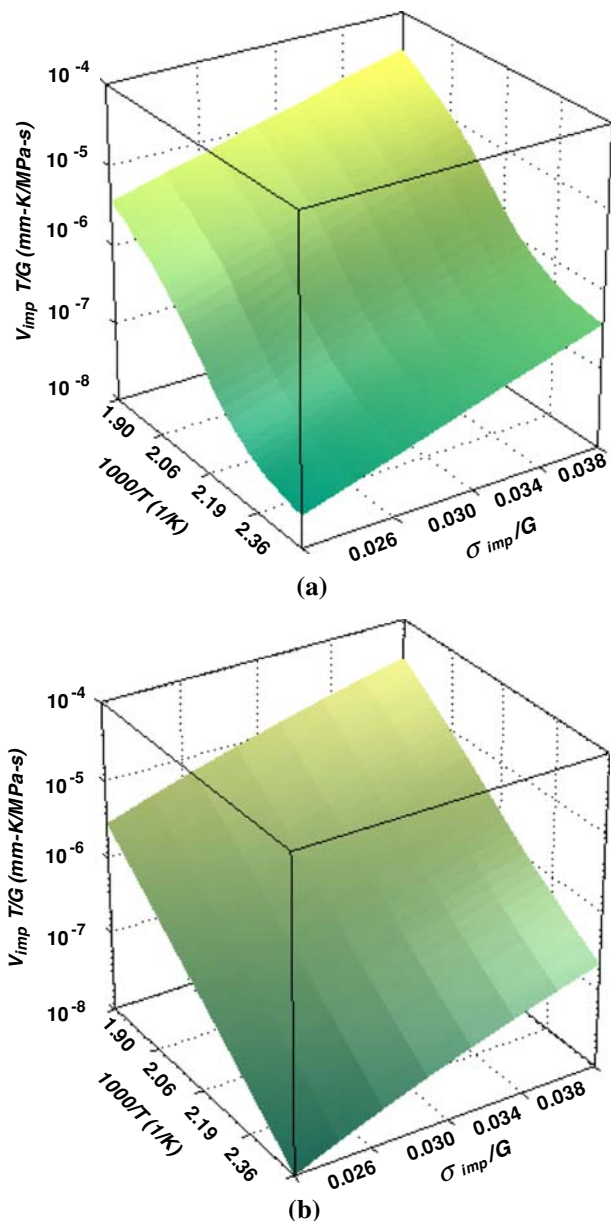
Fig. 10—Three-dimensional plots of the normalized steady-state impression velocity as a function of normalized punching stress and reciprocal temperature for (*a*) AZ91 and (*b*) AZ91-2RE.

IV. CONCLUSIONS

The impression creep test was demonstrated to be capable of evaluating creep behavior of materials using small specimens. The data analyses showed that the simple theory, based on the steady-state power-law creep equation, has the capacity to describe the impression creep data satisfactorily. The structure of AZ91 consists of β-$Mg_{17}Al_{12}$ intermetallic phase in the α-Mg matrix. Due to the low thermal stability of this phase, the creep resistance of AZ91 decreases as the temperature increases. Our results show that the addition of RE elements generally improved the creep resistance of AZ91, mainly due to the formation of $Al_{11}RE_3$ intermetallics. These intermetallic particles are thermally stable barriers that oppose recovery processes, decreasing the minimum creep rates of the materials. The higher creep resistance of the AZ91-2RE alloy is related to the concurrent formation of RE-containing particles, reduction in the volume fraction of β-$Mg_{17}Al_{12}$, and solute hardening effects of Al in the Mg matrix. The stress exponent values, depending on the testing temperature, were in the range of 4.9 to 6.0, 5.6 to 6.8, 5.3 to 6.7, and 6.0 to 7.0 for AZ91, AZ91-1RE, AZ91-2RE, and AZ91-3RE, respectively. The respective activation energies of 94.1 to 112.6 kJ/mol, 90.1 to 118.2 kJ/mol, 96.3 to 110.2 kJ/mol, and 102.0 to 125.8 kJ/mol were obtained for AZ91, AZ91-1RE, AZ91-2RE, and AZ91-3RE at different σ_{imp}/G levels. The change in activation energy with applied stress is indicative of the presence of two parallel creep mechanisms, which we identify as lattice and pipe-diffusion-controlled dislocation climb. Dislocation climb controlled by dislocation pipe diffusion is operant at high stresses, while climb of edge dislocations is the controlling mechanism at low stresses.

$Q_{pd} = 94.5$ kJ/mol is obtained. The fact that our measured activation energy of approximately $Q_c = 95$ kJ/mol, obtained at the high stress ratio of $\sigma_{imp}/G = 0.036$, is very close to that of the dislocation pipe diffusion may imply that the operative creep mechanism under high stress levels is dislocation climb controlled by dislocation pipe diffusion. As the applied stress ratio decreases, the activation energy increases so that it reaches 110.2 and 112.6 kJ/mol for the AZ91-2RE and AZ91, respectively. This means that there would be a transition in the controlling creep mechanism from dislocation climb controlled by dislocation pipe diffusion at high stresses to the lattice-diffusion-controlled climb of edge dislocations at low stresses.

REFERENCES

1. I.J. Polmear: *Light Alloys*, 2nd ed., Chapman and Hall, Inc., New York, NY, 1989, pp. 170–88.
2. A.A. Luo and M.O. Pekguleryuz: *J. Mater. Sci.*, 1994, vol. 29, pp. 5259–71.
3. A.A. Luo: *Int. Mater. Rev.*, 2004, vol. 49, pp. 13–30.
4. M.O. Pekguleryuz and A.A. Kaya: *Adv. Eng. Mater.*, 2003, vol. 512, pp. 866–78.
5. M.S. Dargusch, G.L. Dunlop, and K. Pettersen: *Proc. Conf. on Magnesium Alloys and Their Applications*, Werkstoff-Informationsgesellschaft mbH, Wolsburg, Germany, 1998, pp. 77–82.
6. Y. Guangyin, S. Yangshan, and D. Wenjiang: *Scripta Mater.*, 2000, vol. 43, pp. 1009–13.
7. Y. Guangyin, S. Yangshan, and D. Wenjiang: *Mater. Sci. Eng.*, 2001, vol. A308, pp. 38–44.
8. F. Kabirian and R. Mahmudi: *Adv. Eng. Mater.*, 2009, vol. 11, pp. 189–93.
9. G. Pettersen, H. Westengen, R. Hoier, and O. Lohne: *Mater. Sci. Eng.*, 1996, vol. A207, pp. 115–20.
10. D. Wenwen, S. Yangshan, M. Xuegang, X. Feng, Z. Min, and W. Dengyun: *Mater. Sci. Eng.*, 2005, vol. A356, pp. 1–7.
11. Y. Lu, Q. Wang, X. Zeng, W. Ding, C. Zhai, and Y. Zhu: *Mater. Sci. Eng.*, 2006, vol. A278, pp. 66–75.
12. F. Khomamizadeh, B. Nami, and S. Khoshkhooei: *Metall. Mater. Trans. A*, 2005, vol. 36A, pp. 3489–94.
13. Y. Wang, S. Guan, X. Zeng, and W. Ding: *Mater. Sci. Eng.*, 2006, vol. A416, pp. 109–18.

14. S.N.G. Chu and J.C.M. Li: *J. Mater. Sci.*, 1977, vol. 12, pp. 2200–08.
15. G. Cseh, J. Bar, H.J. Gudladt, J. Lendvai, and A. Juhasz: *Mater. Sci. Eng.*, 1999, vol. A272, pp. 145–51.
16. R. Mahmudi, A.R. Geranmayeh, H. Noori, N. Jahangiri, and H. Khanbareh: *Mater. Sci. Eng.*, 2008, vol. A487, pp. 20–25.
17. D. Dorner, K. Roller, B. Skrotzki, B. Stockhert, and G. Eggler: *Mater. Sci. Eng.*, 2003, vol. A357, pp. 346–54.
18. H. Deming, C. Yungui, T. Yongbai, L. Hongmei, and N. Gao: *Mater. Lett.*, 2007, vol. 61, pp. 1015–19.
19. H. Liu, Y. Chen, Y. Tang, S. Wei, and G. Niu: *Mater. Sci. Eng.*, 2007, vol. A464, pp. 124–28.
20. L.L. Peng, F.Q. Yang, J.F. Nie, and J.C.M. Li: *Mater. Sci. Eng.*, 2005, vols. A410–A411, pp. 42–47.
21. F. Kabirian and R. Mahmudi: *Metall. Mater. Trans. A*, 2009, vol. 40A, pp. 116–27.
22. R. Mahmudi, A.R. Geranmayeh, and A. Rezaee-Bazzaz: *Mater. Sci. Eng.*, 2007, vol. A448, pp. 287–93.
23. W. Blum, Y.J. Li, X.H. Zeng, P. Zhang, B. Von Grossmann, and C. Haberling: *Metall. Mater. Trans. A*, 2005, vol. 36A, pp. 1721–28.
24. K. Ishikawa, H. Watanabe, and T. Mukai: *Mater. Lett.*, 2005, vol. 59, pp. 1511–15.
25. T.G. Langdon: *Proc. 6th Int. Conf. on Strength of Metals and Alloys*, ICSMA 6, R.C. Gifkins, ed., Pergamon Press, New York, NY, 1982, pp. 1105–10.
26. M.D. Mathew, H. Yang, S. Movva, and K.L. Murty: *Metall. Mater. Trans. A*, 2005, vol. 36A, pp. 99–105.
27. T. Reinikainen and J. Kivilahti: *Metall. Mater. Trans. A*, 1999, vol. 30A, pp. 123–32.
28. R. Mahmudi, A. Rezaee-Bazzaz, and H.R. Banaie-Fard: *J. Alloys Compd.*, 2007, vol. 429, pp. 192–97.
29. M. Regev, A. Rosen, and M. Bamberger: *Metall. Mater. Trans. A*, 1998, vol. 32A, pp. 1335–45.
30. J.H. Guo, L.Q. Chen, Y.B. Xu, and F.Z. Lian: *Mater. Sci. Eng.*, 2007, vol. A443, pp. 66–70.
31. N. Ishimatsu, Y. Terada, T. Sato, and K. Ohori: *Metall. Mater. Trans. A*, 2006, vol. 37A, pp. 243–48.
32. O.D. Sherby and P.M. Burke: *Prog. Mater. Sci.*, 1967, vol. 1, pp. 325–90.